PHYSICAL REVIEW E VOLUME 54, NUMBER 5 NOVEMBER 1996

Linear theory of plasma Čerenkov masers

M. Birau
Laboratoire de Physique des Milieux Ionisés, Centre National de la Recherche Scientifique, École Polytechnique,
91128 Palaiseau Cedex, France

(Received 21 March 1996)

A different theoretical model of Čerenkov instability in the linear amplification regime of plasma Čerenkov masers is developed. The model assumes a cold relativistic annular electron beam propagating through a column of cold dense plasma, the two bodies being immersed in an infinite magnetic guiding field inside a perfect cylindrical waveguide. In order to simplify the calculations, a radial rectangular distribution of plasma and beam density is assumed and only azimuthal symmetric modes are under investigation. The model's difference consists of taking into account the whole plasma and beam electromagnetic structures in the interpretation of the Čerenkov instability. This model leads to alternative results such as the possibility of emission at several frequencies. In addition, the electric field is calculated taking into account its radial phase dependence, so that a map of the field in the interaction region can be presented. [S1063-651X(96)03610-0]

PACS number(s): 52.25.Sw, 52.75.Ms, 52.35.Qz

I. INTRODUCTION

Among the diversity of processes that can lead to an efficient transfer of energy from an electron beam to an electromagnetic wave, the Čerenkov instability is based on the ability of a structure to propagate waves with a phase velocity less than the speed of light in the vacuum. In other words, the ''Čerenkov structure,'' more commonly called the ''slow wave structure,'' allows an electron beam to have a velocity greater than the phase velocity of a wave. The wave amplification arises from the interaction of the longitudinal velocity of the electron beam with the longitudinal component of the electric field of the wave.

The first application of this phenomenon in microwave generation was the dielectric Čerenkov maser consisting of a metallic waveguide covered with a thin layer of dielectric [1]. Here the presence of the insulator characterized by a dielectric constant greater than 1 creates the slow wave structure. Schematically, the plasma Čerenkov maser (PCM) consists of replacing the dielectric with a dense plasma. Under these conditions, the dielectric constant becomes a tensor that complicates the analysis. However, one can say that the slow wave structure is permitted by the negative value of the dielectric diagonal term in the longitudinal direction. This phenomenon was explained by Bohm and Gross [2] and Akhiezer and Fainberg [3] when they investigated the general problem of beam-plasma instability. The effect of the magnetic field was taken into account by Stepanov and Kitsenko [4,5]. A significant list of references in this field can be found in the book of Kuzelev and Rukhadze [6].

An efficient use of the Čerenkov instability for the microwave generation in the PCM was demonstrated by Kuzelev *et al.* [7] In that experiment, the relativistic electron beam was fully cylindrical and passed through a cylindrical plasma column. Since then, calculations have shown that an annular electron beam would give a more efficient energy transfer from the beam to the wave to be generated [8]. More PCM prototypes were then built with a diode configuration, leading to an annular electron beam and with a special magnetic-field configuration that permits tuning the plasma column radius. One of these devices emits radiation in the centimeter range on the order of 0.1 GW [9]. The experimental achievement of the PCM is also the result of theoretical investigations. Linear models of the interaction have been developed, among which we may note the studies of Alexandrov *et al.* [10] and Pointon and De Groot [11]. In both cases, the model assumes the interaction to be the result of a monocoupling between the highest phase velocity mode of the slow wave structure (connected to the presence of the plasma in the waveguide) and the so-called slow beam wave mode (connected to the presence of the beam in the waveguide), the whole system being immersed in an infinite magnetic field. In the first case, the model assumes an infinitely thin beam thickness so that the radial slow mode structure connected to the beam annulus in the waveguide is reduced to a unique mode. In the second case, where the beam density is assumed to be sufficiently weak, this structure is reduced also to one mode. The lower phase velocity plasma modes of the slow wave structure are shown to be sufficiently far from the slow beam mode not to interact with it.

Our purpose in this paper is to investigate the interaction between the plasma mode structure and the mode structure induced by the presence of a monoenergetic beam of finite thickness and density in the waveguide. The system will also be assumed to be strongly magnetized in order to simplify calculations. This approach allows the consideration of the multicoupling interaction due to the finite radial geometry of the system.

The structure of the paper is as follows. In Sec. II the theoretical model is developed. This consists of calculating the dielectric tensor in different media, subject to a specific set of assumptions that permit the use of the model. A differential equation governing the longitudinal component of the electric field is obtained and integrated. Boundary conditions applied to the plasma, beam, and waveguide edge yield the linear dispersion relation. The dependence of the growth rate versus plasma density is plotted and discussed.

In Sec. III we focus our attention on the spatial field structure. Phase surfaces of the field components are defined and the field amplitude is plotted on these surfaces. Finally, a

1063-651X/96/54(5)/5599(13)/$10.00

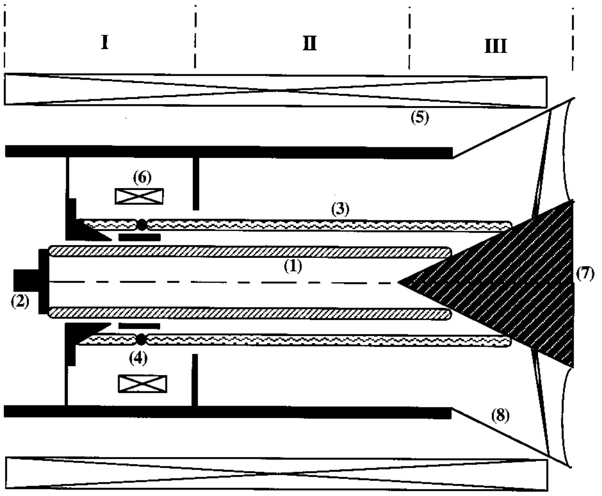

FIG. 1. Experimental setup scheme of the plasma Čerenkov maser: (I), plasma and beam creation zone; (II), interaction zone; and (III), emission zone. The hollow relativistic electron beam (REB) (1) is generated by the explosive cathode (2). The hollow plasma column (3) is created by a discharge obtained after the propagation of a low-energy electron flux from the heated cathode (4) in xenon. The (REB) and plasma are immersed in a strong longitudinal magnetic field (5). An additional coil (6) permits tuning the plasma radius. Both the REB and plasma are lost to the collector (7), which is simultaneously a part of the outlet coaxial horn (8).

field map is presented in the interaction region. In Sec. IV we present a conclusion.

II. THEORETICAL MODEL

The experimental setup of the PCM scheme is presented in Fig. 1. The model will consider only the interaction region, which will be supposed to be infinite in the longitudinal z direction. This assumption can be justified because the amplified wave wavelength is shown to be much less than the interaction region length, which is about 30 cm. However, this assumption prevents us from taking into account the unavoidable feedback due to reflections at the interaction region exit. We consider an annular relativistic electron beam propagating inside an annular column of dense plasma, the ions being sufficiently heavy to be considered at rest. Both the beam and plasma are immersed in a strong longitudinal magnetic field inside a perfectly conducting circular waveguide. The density profile of the two bodies is supposed to be axis symmetric and rectangular along the radius so that the initial-value problem consists of providing eight parameters: inner and outer radii of the plasma and beam, waveguide radius, plasma density or plasma Langmuir frequency, beam current, and energy. The radial section of the system is displayed in Fig. 2.

The theoretical analysis is divided into two parts. First, we consider the waveguide filled with the plasma or the beam column in order to find the eigenmodes of the two systems separately. In a second step, we will consider the plasma and the beam simultaneously to find the nature of the instability that can appear from such a configuration.

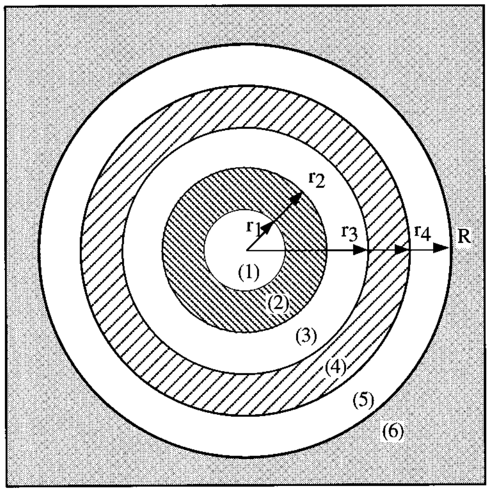

FIG. 2. Radial section of the system in the supposed infinitely long interaction region: r_1, inner beam radius; r_2, outer beam radius; r_3, inner plasma radius; r_4, outer plasma radius; and R, waveguide radius. The beam (plasma) density is constant between r_1 and r_2 (r_3 and r_4).

A. Eigenmodes of a cylindrical waveguide filled with a plasma or a beam

1. Derivation of the dispersion relation

A radial section of the system is presented in Fig. 3. The initial-value problem (without the wave) consists of a cold plasma characterized by its Langmuir frequency ω_p or a cold monoenergetic beam propagating along the z axis with energy E and current I. In both cases, the inner and outer radii of the column will be denoted r_i and r_j, respectively, and the waveguide radius as R. We assume the dependence of the field components to be

$$f(r,\varphi,z,t,k,\omega)=f(r)e^{i(kz-\omega t)} \tag{1}$$

for each point M defined by its cylindrical coordinates r,φ,z. In other words, the field will be assumed to be axis symmetric in the system already supposed to be infinite in the longitudinal direction z. Using linearized equations of motion,

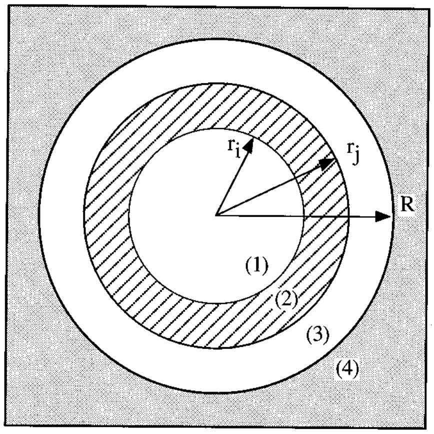

FIG. 3. Radial section of the system filled with plasma or beam: r_i, inner beam (or plasma) radius; r_j, outer beam (or plasma) radius; and R, waveguide radius.

continuity, and Faraday in Fourier-Laplace space, we find the conductivity tensor $\bar{\bar{\sigma}}$ connecting the current density $\mathbf{j}$ and electric field $\mathbf{E}$ according to

$$\mathbf{j}(\mathbf{k},\omega)=\bar{\bar{\sigma}}(\mathbf{k},\omega)\mathbf{E}(\mathbf{k},\omega) \tag{2}$$

and deduce the dielectric tensor defined by

$$\bar{\bar{\varepsilon}}=\bar{\mathrm{I}}-\frac{\bar{\bar{\sigma}}}{i\omega\varepsilon_0}. \tag{3}$$

The details of the calculation and the full expression of the dielectric tensor terms can be found in [12] in a more general case, in the sense that there it is assumed that the field components depend on the azimuthal angle φ and the plasma and beam densities on the radius r. Using its expression and assuming the amplitude of the guiding magnetic field to be sufficiently strong, the expression for the infinite cold plasma or beam dielectric tensor is given by

$$\bar{\bar{\varepsilon}}=\begin{pmatrix}1 & 0 & 0\\ 0 & 1 & 0\\ 0 & 0 & \varepsilon\end{pmatrix} \tag{4}$$

where $\varepsilon=\varepsilon_p=1-\omega_p^2/\omega^2$ in the case of the plasma and $\varepsilon=\varepsilon_b=1-\omega_b^2/\gamma_0^3(\omega-kv_0)^2$ in the case of the beam.

The condition of ''infinite magnetic field'' is not trivial and we will return to this point at the end of the section. The tensor of the infinite media can be applied in our case because the thickness of the plasma and the beam (about 1.0 mm in both cases) is much larger that the corresponding Debye length. As in [12], we include the dielectric tensor in the Faraday and Ampère linearized equations. Using (1), we derive the following six equations governing the field structure in cylindrical coordinates:

$$E_r=K^{-2}\left(-ik\,\frac{\partial E_z}{\partial r}\right),\quad E_\varphi=K^{-2}\left(i\omega\,\frac{\partial B_z}{\partial r}\right),$$

$$B_r=-K^{-2}\left(ik\,\frac{\partial B_z}{\partial r}\right),\quad B_\varphi=-K^{-2}\left(\frac{i\omega}{c^2}\,\frac{\partial E_z}{\partial r}\right), \tag{5}$$

$$\frac{\partial^2 B_z}{\partial r^2}+\frac{1}{r}\,\frac{\partial B_z}{\partial r}+\varepsilon K^2 B_z=0,$$

$$\frac{\partial^2 E_z}{\partial r^2}+\frac{1}{r}\,\frac{\partial E_z}{\partial r}+\varepsilon K^2 E_z=0,$$

where $K^2=k^2-\omega^2/c^2$.

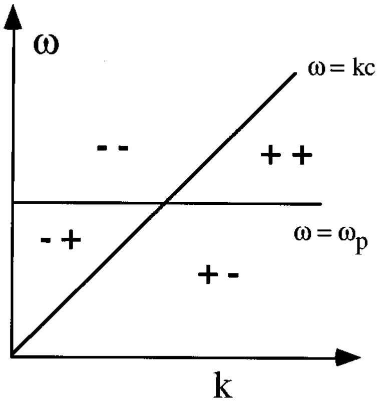

FIG. 4. Respective sign of εK^2 in vacuum and the plasma in the Brillouin diagram for the waveguide partially filled with the plasma.

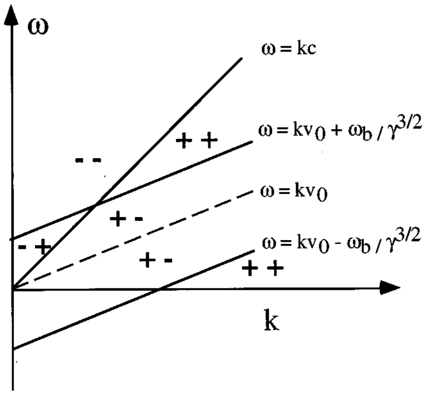

FIG. 5. Respective sign of εK^2 in vacuum and the beam in the Brillouin diagram for the waveguide partially filled with the beam.

The fact that the equations for the E_z and B_z components are linearly independent enables us to define a basis of TM modes (B_z=0) and TE modes (E_z=0). We will focus our attention only on TM modes since the interaction requires a nonzero product $E_z v_z$. Due to the fact that the plasma and beam densities have been assumed to be rectangular along the radius, differential equations present in (5) can be integrated analytically. It should be emphasized that any other profile of plasma or beam density would make impossible an analytic solution of the problem. The integration of the differential equation leads to

$$f(r)=\begin{cases}AJ_0(\sqrt{-\varepsilon K^2}r)+BY_0(\sqrt{-\varepsilon K^2}r) & \text{if } \varepsilon K^2<0,\\ AI_0(\sqrt{\varepsilon K^2}r)+BK_0(\sqrt{\varepsilon K^2}r) & \text{if } \varepsilon K^2>0\end{cases} \tag{6}$$

where J_0 and Y_0 are the Bessel functions of the first and the second kind and I_0 and K_0 the corresponding modified Bessel functions. We see now that for each radius, (6) brings us to study the sign of the real quantity εK^2 in order to determine the form of the solution. This study has been carried out for the waveguide filled with plasma and the waveguide filled with the beam. The sign of εK^2 in vacuum and plasma (Fig. 4) and in vacuum and the beam (Fig. 5), respectively, is shown. The straight lines separate the Brillouin space in four different regions, according to the sign of εK^2

in vacuum and the plasma or the beam. They correspond to zeros of εK^2 and, being the asymptotes of the modes, they describe their behavior for large wave numbers.

As an example, and to illustrate the kind of solution we obtain, we present the radial dependence of the E_z component in the $-+$ region. In the three other regions, the field takes a similar form

$$\begin{aligned} E_{z1}(r) &= A J_0(\sqrt{-K^2}r) \qquad \text{if } 0 \leqslant r \leqslant a, \\ E_{z2}(r) &= B I_0(\sqrt{\varepsilon K^2}r) + C K_0(\sqrt{\varepsilon K^2}r) \qquad \text{if } a \leqslant r \leqslant b, \\ E_{z3}(r) &= D J_0(\sqrt{-K^2}r) + E Y_0(\sqrt{-K^2}r) \qquad \text{if } b \leqslant r \leqslant R. \end{aligned} \tag{7}$$

Equations (7) depend on five different constants A, B, C, D, and E. So far, we have considered the spatial regions as infinite and independent from each other, which explains the high degree of freedom of the system. In order to reduce it to one, we must apply the boundary conditions to the electromagnetic field at each frontier of the plasma or beam and at the edge of the waveguide. It comprises the continuity of the tangential component of the electric field and the continuity of the normal component of the electric displacement $\mathbf{D}=\bar{\bar{\varepsilon}}\mathbf{E}$ at each surface. However, at the waveguide frontier, only the first condition remains because the dielectric tensor of the perfect metal is undefined. Using the properties of the Bessel functions, we find four systems of five linear algebraic equations with five unknown quantities. By setting each determinant of the four systems to zero, which rejects the trivial solution $E_z=0$, we derive the dispersion relation connecting k and ω. The determinant corresponding to the $-+$ region is given by

$$\begin{vmatrix} J_0(\sqrt{-K^2}r_i) & -I_0(\sqrt{\varepsilon K^2}r_i) & -K_0(\sqrt{\varepsilon K^2}r_i) & 0 & 0 \\ J_1(\sqrt{-K^2}r_i) & \sqrt{-\varepsilon}I_1(\sqrt{\varepsilon K^2}r_i) & -\sqrt{-\varepsilon}K_1(\sqrt{\varepsilon K^2}r_i) & 0 & 0 \\ 0 & I_0(\sqrt{\varepsilon K^2}r_j) & K_0(\sqrt{\varepsilon K^2}r_j) & -J_0(\sqrt{-K^2}r_j) & -Y_0(\sqrt{-K^2}r_j) \\ 0 & \sqrt{-\varepsilon}I_1(\sqrt{\varepsilon K^2}r_j) & -\sqrt{-\varepsilon}K_1(\sqrt{\varepsilon K^2}r_j) & J_1(\sqrt{-K^2}r_j) & Y_1(\sqrt{-K^2}r_j) \\ 0 & 0 & 0 & J_0(\sqrt{-K^2}R) & Y_0(\sqrt{-K^2}R) \end{vmatrix} = 0. \tag{8}$$

We return now to the assumption of infinite magnetic field used in the model. The condition defining the validity of the assumption is not trivial since it requires conducting an analysis using the general dielectric tensor with finite magnetic field and comparing both results. An analysis carried out in a finite magnetic field but in the framework of infinitely thin plasma and beam thickness [13] showed that the assumption of infinitely magnetic field is valid as long as

$$\Omega_0 \gg \frac{\omega_p^2(r_j-r_i)(r_i+r_j)}{2Rc}, \tag{9}$$

where Ω_0 is the cyclotron frequency. This inequality is constraining for high plasma densities that require a high magnetic-field amplitude.

2. Results

A search for the zeros of the expression $D(k,\omega)=0$ is conducted numerically. For each k and by linear interpolation, we find the frequencies ω that satisfy the dispersion relation. This method, though time consuming, has the merit of being simple and rigorous. The results are presented in Fig. 6 for the plasma and in Fig. 7 for the beam. The calculation has been performed using the following parameters, which are characteristic of our experimental setup: inner radius of the beam, 0.50 cm; outer radius of the beam, 0.60 cm; inner radius of the plasma, 0.85 cm; outer radius of the plasma, 0.95 cm; radius of the waveguide, 1.80 cm; plasma Langmuir frequency, 3.0×10^{11} rad s^{-1};beam energy, 511 keV; and beam current, 3.2 kA. As expected, both systems are stable since for every mode able to exist, no point can be found where $dk/d\omega=0$ [14]. Because of this, for each real value of k correspond real values of ω that permit us to develop the analysis in real (k,ω) space only.

Though the diagram of the plasma system has been known from a long time [15], developing the model was necessary for the next step, which treats the coupling. The plot (Fig. 6) shows typical modes of the empty waveguide above the dashed line $(\omega=kc)$ slightly shifted to a higher frequency by the presence of the plasma. Nevertheless, their nature remains the same since their phase velocity is greater than c. Another type of modes under the line $\omega=kc$ is present. These modes have the desirable property of having a phase velocity smaller than c. Let us note also that their number is infinite, their density growing as the ratio kc/ω increases. These modes have been named ''nonresonant'' or surface waves because their corresponding field is strongly confined in the vicinity of the plasma. Finally, it is worth noting the even character of ε and K^2 with respect to k and ω. Due to the form of the dispersion relation (8), this even character is directly transmitted to the implicit function $D(k,\omega)=0$. Namely, if (k,ω) is a solution of the dispersion relation, the three couples $(k,-\omega)$, $(-k,\omega)$, and $(-k,-\omega)$ are also solutions.

Now, let us examine the result for the beam (Fig. 7). This diagram is the Lorentz transformation of a diagram characterizing a plasma instead of the beam with the same density

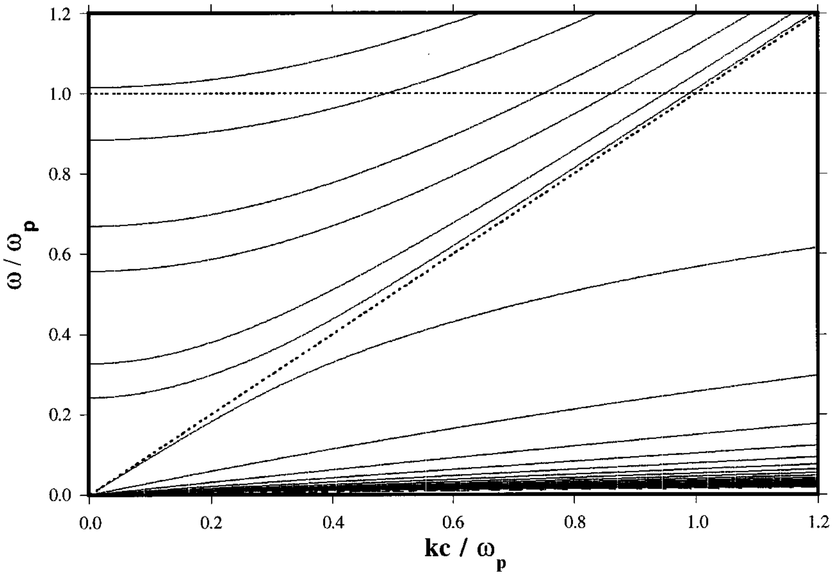

FIG. 6. Dispersion relation for the waveguide filled with plasma. The parameters of the calculation are $r_i=0.85$ cm, $r_j=0.95$ cm, $R=1.80$ cm, and $\omega_p=3.0\times10^{11}$ rad s^{-1}. The dashed lines represent $\omega=\omega_p$ and $\omega=kc$.

(since the Langmuir frequency is an invariant to the Lorentz transformation) and the same geometrical parameters. Its topology has obvious similarity to the previous one. We again encounter the empty waveguide modes; the frequency shift due to the presence of the beam is, however, weaker in this case. The modes that were localized at the vicinity of the line $\omega=0$ between ω_p and $-\omega_p$ are now confined between the lines $\omega=kv_0+\omega_b/\gamma^{3/2}$ and $\omega=kv_0-\omega_b/\gamma^{3/2}$. Note that in the shown region (which is the interesting one, as we will see later), the first slow beam mode (with lowest phase velocity) is sufficiently far from the line $\omega=kv_0$ and from the asymptotic limit $\omega=kv_0-\omega_b/\gamma^{3/2}$ to be distinguished from these two values; thus an identification of this mode with these lines is not desirable. On the other hand, this mode is not alone and we are dealing with an infinite number of them. This structure is due to the pseudoperiodicity of the Bessel functions and expresses the finite thickness and non-negligible density of the beam. On the scale of the graph, the two first modes can be distinguished despite the fact that, in comparison to the plasma diagram, their density is much higher. This highest mode density is due to the lower value of the beam density and to the relativistic factor γ, which brings together the two asymptotic lines between which the modes are localized.

B. Coupling of the structures

1. Derivation of the dispersion relation

We consider now the presence of plasma and the beam simultaneously in the waveguide, which means the coupling of the two previously studied structures (Fig. 2). The process of the analysis is identical to the study of the eigenmodes. The difference is that instead of two kinds of media (vacuum-plasma or vacuum-beam), we are dealing now with three kinds (vacuum-plasma-beam). We will not consider the case where the beam and the plasma overlap in the same radial region. Consequently, the Brillouin diagram can be subdivided into eight distinguished regions corresponding to a given sign of εK^2 in different media. Three kinds of diagrams exist depending on the value of the ratio ω_b/ω_p and the relativistic factor γ. These zones are indicated in Fig. 8 for the case where $\omega_b/\omega_p<\gamma^{3/2}(1-v_z/c)$. As previously

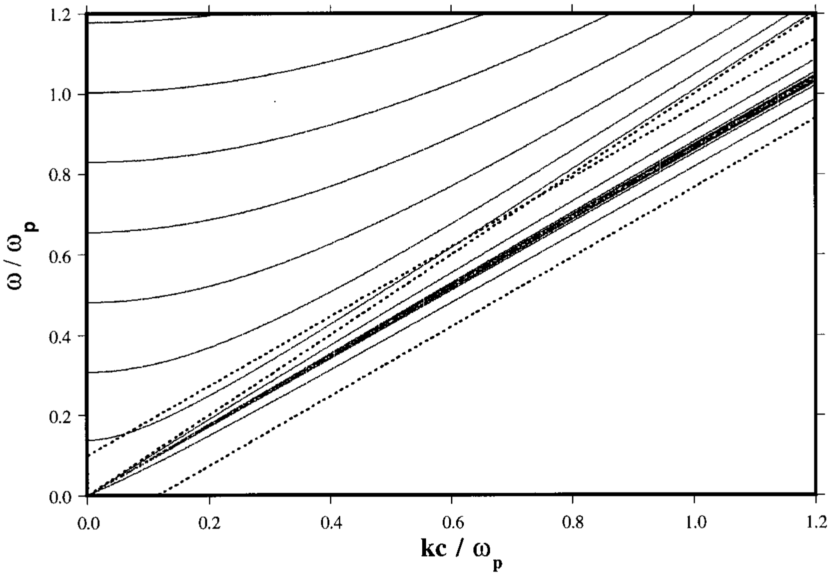

FIG. 7. Dispersion relation for the waveguide filled with the beam. The parameters of the calculation are $r_i=0.50$ cm, $r_j=0.60$ cm, $R=1.80$ cm, $E=511$ keV, and $I=3.2$ kA. Dashed lines represent $\omega=kv_0\pm\omega_b/\gamma^{3/2}$ and $\omega=kc$.

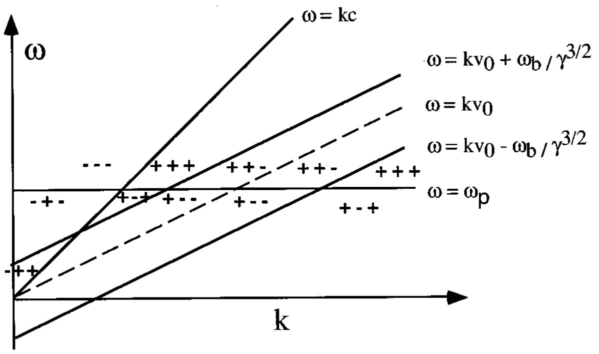

FIG. 8. Respective sign of εK^2 in vacuum, the plasma, and the beam in the Brillouin diagram for the waveguide filled with both plasma and the beam.

done, we present the radial dependence of the E_z component in one of the eight Brillouin diagram regions. We have chosen the $+--$ region, which hence corresponds to a positive value of εK^2 in the vacuum and a negative value of εK^2 in the plasma and beam:

$$E_{z1}(r)=AI_0(\sqrt{K^2}r)\quad \text{if } 0\leqslant r\leqslant r_1, \tag{10}$$

$$E_{z2}(r)=BJ_0(\sqrt{-\varepsilon_b K^2}r)+CY_0(\sqrt{-\varepsilon_b K^2}r)$$
$$\text{if } r_1\leqslant r\leqslant r_2,$$

$$E_{z3}(r)=DI_0(\sqrt{K^2}r)+EK_0(\sqrt{K^2}r)\quad \text{if } r_2\leqslant r\leqslant r_3,$$

$$E_{z4}(r)=FJ_0(\sqrt{-\varepsilon_p K^2}r)+GY_0(\sqrt{-\varepsilon_p K^2}r)$$
$$\text{if } r_3\leqslant r\leqslant r_4,$$

$$E_{z5}(r)=HI_0(\sqrt{K^2}r)+IEK_0(\sqrt{K^2}r)\quad \text{if } r_4\leqslant r\leqslant R,$$

where r_1,r_2 are the inner and outer beam radii, r_3,r_4 the inner and outer plasma radii, and the index b or p of ε indicates the beam or plasma medium. Instead of five constants, the form of the field makes nine constants appear, A to I. The boundary conditions applied at each edge of the plasma and beam and at the edge of the waveguide form an algebraic linear system of nine equations with nine unknown quantities. Setting each determinant of the eight systems to zero yields the dispersion relation. It appears in the form of eight 9×9 determinants. The determinant corresponding to the $+--$ region is

$$\begin{vmatrix}
I_0(\chi r_1) & -J_0(\mu\chi r_1) & -Y_0(\mu\chi r_1) & 0 & 0 & 0 & 0 & 0 & 0\\
I_1(\chi r_1) & \mu J_1(\mu\chi r_1) & \mu Y_1(\mu\chi r_1) & 0 & 0 & 0 & 0 & 0 & 0\\
0 & J_0(\mu\chi r_2) & Y_0(\mu\chi r_2) & -I_0(\chi r_2) & -K_0(\chi r_2) & 0 & 0 & 0 & 0\\
0 & \mu J_1(\mu\chi r_2) & \mu Y_1(\mu\chi r_2) & I_1(\chi r_2) & -K_1(\chi r_2) & 0 & 0 & 0 & 0\\
0 & 0 & 0 & I_0(\chi r_3) & K_0(\chi r_3) & -J_0(\nu\chi r_3) & -Y_0(\nu\chi r_3) & 0 & 0\\
0 & 0 & 0 & I_1(\chi r_3) & -K_1(\chi r_3) & \nu J_1(\nu\chi r_3) & \nu Y_1(\nu\chi r_3) & 0 & 0\\
0 & 0 & 0 & 0 & 0 & J_0(\nu\chi r_4) & Y_0(\nu\chi r_4) & -I_0(\chi r_4) & -K_0(\chi r_4)\\
0 & 0 & 0 & 0 & 0 & \nu J_1(\nu\chi r_4) & \nu Y_1(\nu\chi r_4) & I_1(\chi r_4) & -K_1(\chi r_4)\\
0 & 0 & 0 & 0 & 0 & 0 & 0 & I_0(\chi R) & K_0(\chi R)
\end{vmatrix}=0, \tag{11}$$

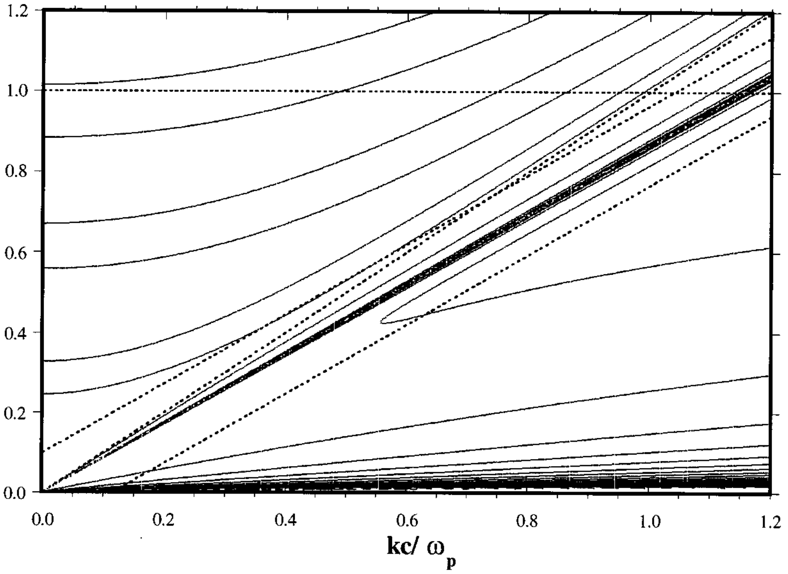

FIG. 9. Dispersion relation in real space for the waveguide filled with the beam and plasma. The parameters of the calculation are $r_1=0.50$ cm, $r_2=0.60$ cm, $E=511$ keV, $I=3.2$ kA, $r_3=0.85$ cm, $r_4=0.95$ cm, $\omega_p=3.0\times 10^{11}$ rad s^{-1}, and $R=1.80$ cm. The dashed lines represent the lines $\omega=\omega_p$, $\omega=kv_0\pm\omega_b/\gamma^{3/2}$, and $\omega=kc$.

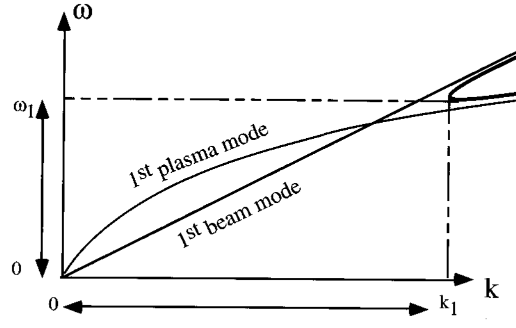

FIG. 10. Superimposition diagram of both coupled (heavy line) and uncoupled (thin lines) modes in the case of a unique coupling.

where for readability we have defined the quantities

$$\chi = \sqrt{K^2}, \quad \mu = \sqrt{-\varepsilon_b}, \quad \nu = \sqrt{-\varepsilon_p}. \tag{12}$$

2. Results in real space

The result of the plasma and beam structure coupling in real Brillouin space is presented in Fig. 9. The beam and plasma parameters are those used in Sec. II A 2. Let us focus our attention on the lowest phase velocity mode of the beam mode structure (called the first beam mode) and on the highest phase velocity mode of the plasma structure (called the first plasma mode). These two modes differ little from the uncoupled ones for large values of k and ω. To fully under stand the diagram, these two modes and their coupling have been superimposed in Fig. 10. Clearly these modes are coupled for wave numbers between a value very near 0 and k_1, corresponding to the disappearance of the curves in the real diagram, the frequency becoming complex in this region. The point $k = k_1$ satisfies $dk/d\omega = 0$. The existence of the point $\omega = \omega_1$ defined by $d\omega/dk = 0$ shows that we are dealing with a convective instability. This instability that takes place in the $+--$ region defined previously is allowed by the negative sign of the longitudinal diagonal term of the dielectric tensor in the plasma and the beam. The uncommon wideband instability feature can be explained by considering the topology of the uncoupled modes. These are indeed very close to each other all along the instability wave numbers so that the instability takes place on a very large range. For a lower coupling, one could expect an island to appear between the two uncoupled modes in the instability region leading to a splitting of the instability on two different frequencies. However, we did not observe such a splitting. Instead of this, a multicoupling configuration takes place as shown in Fig. 11, obtained for a highest plasma density. The coupling topology is explained in Fig. 12, where three uncoupled modes have been superimposed with the dispersion relation itself: the first plasma mode (with the highest phase velocity) and the two first slow beam modes (with the lowest phase velocity). Four different regions of the Brillouin diagram can be distinguished. Starting from low values of k and ω, the coupling begins between the first plasma mode and the second beam mode (k varying from 0 to k_1). Then for each real k between k_1 and k_2, three real values of ω corresponding to each considered mode are present so that in this range the configuration is stable. Another instability due to the coupling of the same plasma mode with the first slow beam mode can be seen from k_2 to k_3. Finally, for larger wavenumber values, the configuration is stable. The parameters used for Figs. 11 and 12 have lead to a coupling between the first plasma mode and the two first slow beam modes. For a lower beam energy, we have obtained other coupling configurations including other beam and plasma modes so that the instability splitting takes place on more than two frequencies, as shown in Fig. 13.

3. Results in complex space: Growth rate of the instability

The analysis conducted up to now in the real space informs us about the instability spectrum width without giving its amplitude. In order to estimate the consequences for the emission spectrum it is necessary to calculate the complex

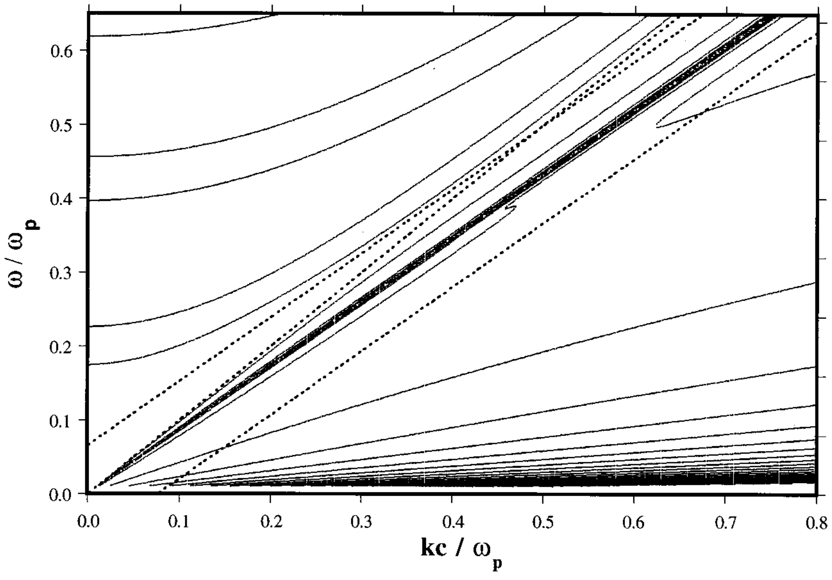

FIG. 11. Dispersion relation in real space for the waveguide filled with the beam and plasma. The parameters are identical to those used in Fig. 9, except for the plasma density, which has been increased to $\omega_p = 4.5 \times 10^{11}$ rad s^{-1}.

frequency that will satisfy the differential equation (5) in complex space. The distinction of the solutions based on the sign of εK^2, which is necessary in real space, here becomes obsolete and we may write the solution

$$f(r)=AJ_0(\sqrt{-\varepsilon K^2 r})+BY_0(\sqrt{-\varepsilon K^2 r}), \tag{13}$$

where J_0 and Y_0 are Bessel functions of the first kind with a complex argument. Following the same analysis as in real space, one comes to the dispersion relation, which has a form similar to expression (11) and the terms of the determinant are complex. Noting the frequency $\omega=\omega_r+i\omega_i$, the problem involves finding the three real roots k,ω_r,ω_i of the complex expression $D(k,\omega_r,\omega_i)=0$. The method that could be applied in the two-dimensional real-space analysis consisting of systematically sweeping the Brillouin diagram manifestly cannot be applied in a three-dimensional volume for calculation time reasons. To search for the roots, we have applied for fixed k the iterative Newton method to the Taylor-series expansion in ω of the dispersion function defined by $D(k,\omega)=0$ [16,17]. The order of the development has been chosen equal to 2. Noting the step $\Delta_n=\omega_{n+1}-\omega_n$, the series defined by

$$\begin{aligned}D(k,\omega_{n+1})=D(k,\omega_n)&+\left[\frac{\partial D(k,\omega_n)}{\partial\omega}\right]_{\omega=\omega_n}(\Delta_n)\\&+\frac{1}{2}\left[\frac{\partial^2 D(k,\omega_n)}{\partial\omega^2}\right]_{\omega=\omega_n}(\Delta_n)^2\end{aligned} \tag{14}$$

is convergent, n being the number of iterations already performed. Assuming $D(k,\omega_{n+1})=0$, one obtains from (14)

$$\begin{aligned}\Delta_n=&-\frac{[\partial D(k,\omega)/\partial\omega]_{\omega=\omega_n}}{[\partial^2 D(k,\omega)/\partial\omega^2]_{\omega=\omega_n}}\\&\times\left[1-\sqrt{1-2D(k,\omega_n)\,\frac{[\partial^2 D(k,\omega)/\partial\omega^2]_{\omega=\omega_n}}{[\partial D(k,\omega)/\partial\omega]^2_{\omega=\omega_n}}}\right].\end{aligned} \tag{15}$$

Then one may iterate again until the required precision is obtained. The real-space analysis gives the initialization of ω for the largest value of k. For the next lower wave numbers, linear interpolation is used.

Figure 14 presents the result of calculations for different plasma densities achievable in our experiment. The horizontal scale is the frequency in gigahertz. The vertical scale is the growth rate in power expressed in decibels after a run of 30 cm. The time growth rate has been transformed into spatial growth rate as usual using the formula

$$k_i=\frac{\omega_i}{\left(\dfrac{\partial\omega_r}{\partial k}\right)}. \tag{16}$$

Depending on the amplitude of the plasma density, two situations appear. For low plasma density [curves (1)–(5) with open markers], the instability spectrum is localized on a unique frequency. When plasma density increases, the spectrum band extends from 0 to a higher frequency to reach about 20 GHz for the last curve. The topmost value of the amplitude also increases to reach the appreciable value of about 70 dB (corresponding to an increment of 5.6×10^9 rad s^{-1}) if we compare to other devices such as a dielectric Čerenkov maser [18] or corrugated waveguide fulfilled with plasma [19]. For higher plasma densities [curves (6)–(9) with closed markers], the spectrum splitting due to the coupling of the first plasma mode with several slow beam modes appears as we previously mentioned in the real-space analysis. When plasma density increases, the increment of the main coupling diminishes and the spectrum narrows and shifts to higher frequencies. The secondary couplings have slowly growing amplitude and follow the frequency shifting of the main coupling.

4. Comparison with previous calculations, simulations, and experimental measurements

As mentioned in the Introduction, previous linear models have been developed in the case of a monocoupling between the fastest plasma mode and the slow beam wave [8,11,20]. Two cases can be distinguished depending on the physical parameters of the problem: if only the first slow beam wave interacts with the fastest plasma wave, our instability spectrum coincides correctly with the spectrum calculated by previous models; if higher-order beam modes are involved in the process, the main coupling instability coincides also, but our model is the only one to take into account the secondary instabilities.

It is now of interest to study the possibility of emission of these new modes. The simplest approach is to consider the effect of the axial boundary conditions, which result in the reflection of the wave in the longitudinal direction. As a result, only frequencies with a sufficient growth rate can be amplified. Indeed, for each real frequency ω_r the amplification that is only a necessary condition for emission requires

$$R_1R_2k_iL>1, \tag{17}$$

where R_1,R_2 are the reflection coefficients at each longitudinal boundary of the interaction region, k_i is the spatial growth rate of the frequency ω_r, and L is the interaction region length. Assuming $R_1=1$ and $R_2=0.25\gamma^{-2}$ [21], including experimental parameters into (17) ($L=30$ cm and $\gamma=2$) and using (16), we obtain an amplification threshold of the frequencies corresponding to a growth rate at a power of 13 dB. Because this value is very close to the topmost value of the secondary couplings (Fig. 13), it is difficult to conclude from this approach if these instabilities are amplified or damped.

The problem of the maser ability to emit the instability spectrum can only be strictly treated in the framework of a nonlinear analysis. In this field, we may note the self-consistent particle model, cylindrical symmetry, TM modes, and plasma (CYLTMP) developed in order to treat the nonlinear stage of amplification [11]. Purely nonlinear results provided by this analysis such as power and efficiency can-

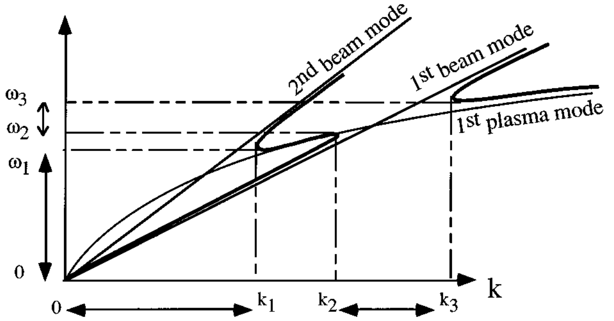

FIG. 12. Superimposition diagram of both coupled (heavy line) and uncoupled (thin lines) modes in the case of a double coupling.

not be compared to linear outcomes. However, the growth rate of several frequencies can be calculated before saturation and has been shown to be in good agreement with previous calculations. Unfortunately, all the available results performed by using this code have been obtained only for configurations leading to a unique coupling [8,11]. Higher-order modes of the beam or plasma remain passive and because in this case our linear model coincides with the previous one, it coincides also with the simulations. Other configurations with, for example, a higher plasma Langmuir frequency would be required to excite the new modes. Such simulations could give information about the behavior of these secondary couplings in the nonlinear stage of amplification.

Measurements of the spectrum have been carried out with the beam and geometrical parameters close to those we have used for the calculation. Figure 15, taken from [20], displays the experimental spectrum for different plasma Langmuir frequencies between 0.9 and 4.0×10^{11} rad s^{-1}. The comparison of these experimental results with our linear calculations has to be made carefully. At first, the measured spectrum is nonlinear, which means that nonlinear processes appears and as a result, it is possible that the power spectrum is not proportional to the growth rate spectrum. Note also that our model does not take into account several characteristics of the experiment such as the finite magnetic field and the finite length of the experimental setup. Finally, the experimental parameters are defined with a finite accuracy.

In this experiment the spectrometer was sensitive only in the 8–17.3 GHz band. For each of the five measured frequencies, the height of each vertical line is proportional to the power received with a bandwidth of 10%. Many characteristics of the spectrum behavior are in good agreement with our calculations: up to $\omega_p = 1.8 \times 10^{11}$ rad s^{-1}, the emission frequency is under the sensitive frequency band of the spectrometer. In the calculations, the spectrum reaches this sensitive zone for a Langmuir frequency between 1.5 and 2.0×10^{11} rad s^{-1}. Then, up to $\omega_p = 2.5 \times 10^{11}$ rad s^{-1}, the spectrum widens out and the midband frequency increases with the plasma density. This tendency is also observed in the calculations. The splitting of the spectrum on both frequencies appears for $\omega_p = 2.5 \times 10^{11}$ rad s^{-1}, whereas in the calculation it takes place in the vicinity of $\omega_p = 3.5 \times 10^{11}$ rad s^{-1}. For higher plasma densities, a great part of the spectrum is out of range of the spectrometer band.

From this comparison, we can conclude that our calculations are in reasonable agreement with the experimental spectrum. The multicoupling of the plasma-beam modes observed in the linear model seems to be the reason for the emission spectrum on at least two frequencies for sufficiently high plasma density. Because of the different inherent meaning of experimental and theoretical spectra mentioned above, it is not possible to be more categorical.

III. FIELD STRUCTURE

From the previous analysis, the dispersion relation of the system is known, that is to say, the complex frequencies ω able to propagate and grow for each real wave number k. Because of the wideband spectrum, the field structure depends on the wave number so that an eigenfield structure corresponds to each generated frequency of the band spectrum. The global field structure is a superimposition of the configuration corresponding to each frequency. However that may be, we suppose that the structure of the field corresponding to different frequencies are of the same nature so that the analysis is conducted with a unique frequency. We have chosen the frequency with the topmost growth rate value to emphasize the effect of amplification on the field structure. All the following results have been conducted with

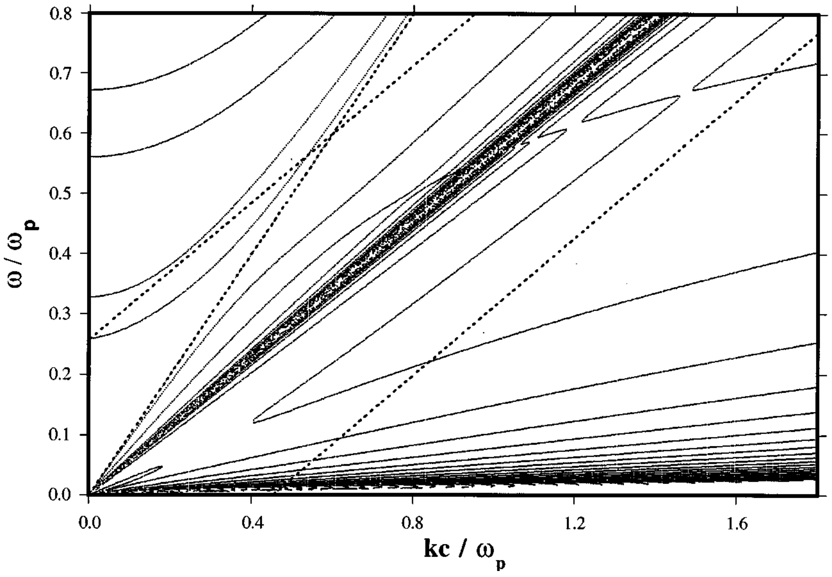

FIG. 13. Dispersion relation in real space for the waveguide filled with the beam and plasma. The parameters are identical to those used in Fig. 9, except for the beam energy, which has been decreased to 111 keV.

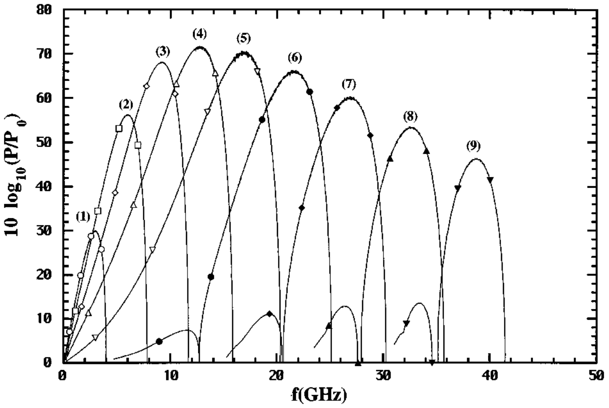

FIG. 14. Growth rate of the instability expressed in power in decibel scale after a run of 30 cm versus the frequency for different Langmuir frequencies. The parameters of the calculation are $r_1=0.50$ cm, $r_2=0.60$ cm, $E=511$ keV, $I=3.2$ kA, $r_3=0.85$ cm, $r_4=0.95$ cm, $R=1.80$ cm, (1) $\omega_p=1.0\times10^{11}$ rad s^{-1}, (2) $\omega_p=1.5\times10^{11}$ rad s^{-1}, (3) $\omega_p=2.0\times10^{11}$ rad s^{-1}, (4) $\omega_p=2.5\times10^{11}$ rad s^{-1}, (5) $\omega_p=3.0\times10^{11}$ rad s^{-1}, (6) $\omega_p=3.5\times10^{11}$ rad s^{-1}, (7) $\omega_p=4.0\times10^{11}$ rad s^{-1}, (8) $\omega_p=4.5\times10^{11}$ rad s^{-1}, and (9) $\omega_p=5.0\times10^{11}$ rad s^{-1}.

a Langmuir frequency of 3.0×10^{11} rad s^{-1} for an emission frequency of 16.3 GHz.

The assumptions made in our model with the Maxwell equations (5) lead to

$$E_r=-ikK^{-2}\left(\frac{\partial E_z}{\partial r}\right),\quad E_\varphi=0,$$

$$B_r=0,\quad B_\varphi=\frac{\omega}{kc^2}E_r,\quad B_z=0. \tag{18}$$

The magnetic field is purely azimuthal and presents a dephasing φ_ω with respect to the radial component of the electric field because of the complex character of the frequency ω. This dephasing is constant all along the radius and is given by

$$\varphi_\omega=\arctan\left(\frac{\omega_i}{\omega_r}\right). \tag{19}$$

This complex character also becomes apparent in the radial field dependence $f(r)$ defined in (1) so that it can be written $f(r)=|f(r)|e^{i\varphi(r)}$ and the real components of the field appear under the form of a three-term product

$$e^{\omega_i t}|f(r)|\cos[kz-\omega_r t+\varphi(r)]. \tag{20}$$

These terms are, respectively, the temporal growth rate, the radial dependence of the amplitude, and the oscillatory term, which depends on the radius. The radial dependence of each field component is hence described by its own two parameters: the amplitude $|f(r)|$ and the phase $\varphi(r)$. Noting that $\varphi_r(r)$ and $\varphi_z(r)$ represent the radial dephasing of the radial and longitudinal component of the electric field, we define the quantities

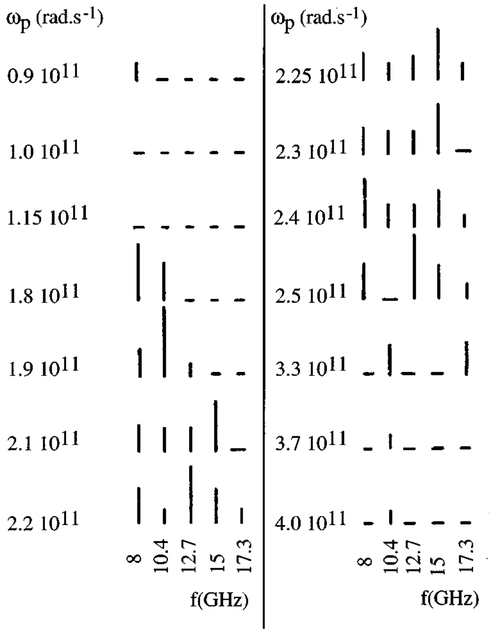

FIG. 15. Experimental radiation spectra for different plasma Langmuir frequencies taken from [20]. The parameters used in the experiment are the average radius of the hollow beam, $r_b=0.60$ cm; the average radius of the plasma column, $r_p=0.80$ cm; the waveguide radius, $R=1.80$ cm; the beam energy, $E=650$ keV; the beam current, $I=3$ kA; and the guiding magnetic field, $B=2.0$ T.

$$z_r(r)=\frac{\varphi_r(r)}{k},\quad z_z(r)=\frac{\varphi_z(r)}{k}, \tag{21}$$

which describe the wave surface of the component. These values are plotted along the radius in Fig. 16 on a scale of the amplified wavelength. The picture shows strongly undulated surfaces, particularly for the radial component. The phase change occurs strongly inside the plasma and the beam. The physical meaning of these surfaces can be understood by considering the Poynting vector. Indeed, using expressions (18)–(21), its real components can be written

$$\mathbf{S}=\frac{\mathbf{E}\times\mathbf{B}}{\mu_0}=\begin{pmatrix}S_r\\0\\S_z\end{pmatrix},$$

where

$$S_r=-\frac{e^{2\omega_i t}|\omega|}{2\mu_0kc^2}|E_z(r)||E_r(r)|(\cos\{2(kz-\omega_r t)+k[z_r(r)+z_z(r)]+\varphi_\omega\}+\cos\{k[z_r(r)-z_z(r)]+\varphi_\omega\}),$$

$$S_z=\frac{e^{2\omega_i t}|\omega|}{2\mu_0kc^2}|E_r^2(r)|[\cos(2\{k[z+z_r(r)]-\omega_r t\}+\varphi_\omega)+\cos(\varphi_\omega)]. \tag{22}$$

Hence, for each value of the radius, the energy flux components can be written as a superimposition of an oscillatory term in (z,t) and a constant term. The oscillatory term has a zero average value in time and permits the definition of the two surfaces for which the phase of energy flux in the radial and the longitudinal direction is constant. The $z_r(r)$ surface

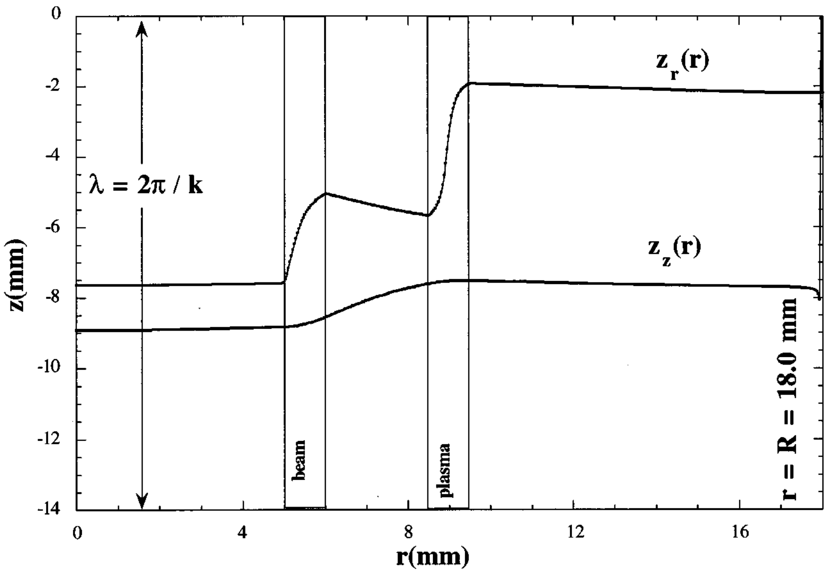

FIG. 16. Wave surfaces of the longitudinal and radial electric-field components versus the radius.

corresponds to the same phase of power density transmission in the longitudinal direction. The surface that we call $\chi_r(r)$, corresponding to the same phase of power density transmission in the radial direction, is defined by

$$\chi(r) = -\frac{z_r(r)+z_z(r)}{2} - \frac{\varphi_\omega}{2k}. \tag{23}$$

The amplitude of the field is plotted in Fig. 17. We must emphasize that these curves have been plotted along the wave surfaces defined previously because they are the only ones that are representative of the physical geometry of the problem. The figure shows two maxima for the longitudinal component and inversely a drop in the radial component in these media. The phenomenon is more pronounced in the plasma since its density is stronger than that of the beam. Also, one can verify that the boundary condition on the metal edge is strictly observed since the longitudinal component drops to zero for this radius. The basic process of the interaction is localized in the beam crown where the transfer of kinetic energy to the radiation takes place. Nevertheless, because of the boundary conditions, an increase of E_z in the beam region due to the transfer of energy leads to the growth of both components in the whole radial space, as shown on the graph.

We now turn to the question of energy transport by means of a Poynting vector. Figure 18 describes its components in the radial and the longitudinal direction. The two curves have been plotted along the surfaces $z_r(r)$ and $\chi_r(r)$ described previously. Because of the presence of the waveguide, the radial component cannot be emitted and one can verify that its value is zero at this boundary. Most of it is concentrated in the beam-plasma crown and describes the exchange of energy from the beam to the plasma. The longitudinal component that describes the extractable power is almost zero inside the beam, reaches a high level between beam and plasma, has its maximum value at the outer edge of the plasma, and decreases to a value near zero at the metal

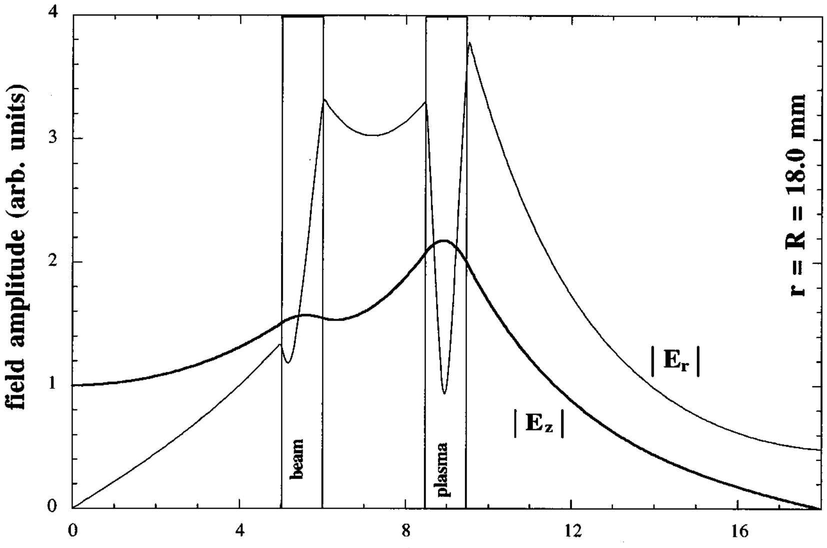

FIG. 17. Distribution of the longitudinal and radial electric-field amplitudes along the radius.

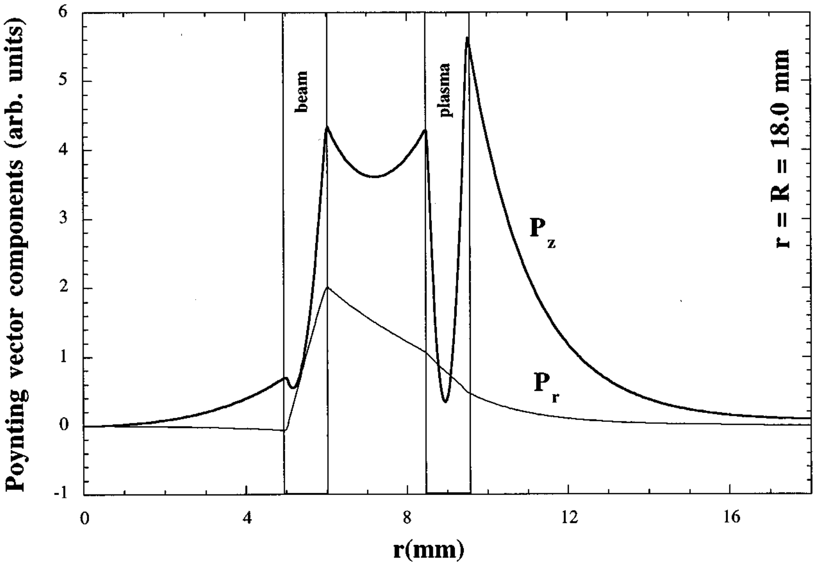

FIG. 18. Radial distribution of the longitudinal and radial Poynting vector components.

edge. Note that because of the collector presence located at the end of the tube interaction region (Fig. 18), radiation can be easily extracted only from the vacuum annulus between the plasma and metal. Radiation from inside undergoes a very high attenuation when crossing the plasma and possibly the beam, so that it is mostly reflected.

The next graph shows the field lines of the system at the scale of a wavelength in the interaction region (Fig. 19). The frequency of the wave is conserved from the interaction region to the coaxial emitting zone, so the corresponding emitted wavelength will be modified by a factor corresponding to the wave phase velocity ratio between these two regions. The density of the field lines corresponds as usual to the field amplitude. The picture shows a classical profile of the TM01 mode inside the beam, which plays the role of the metal. However, the field lines are not strictly perpendicular to it. In the two others regions (beam-plasma and plasma-metal), the field lines have a particular configuration since some lines leaving the plasma return to it while others go up to the metal or the beam. We did not draw the field lines inside the beam and the plasma because of their weak amplitude. One can note that where its amplitude strongly drops, the field is longitudinally oriented.

IV. CONCLUSION

We have presented in this paper a linear model of the interaction in the plasma Čerenkov maser. Several assumptions have been made to carry out the analysis: the assumption of infinite media in the longitudinal direction, the assumption of infinite guiding magnetic field, the assumption of rectangular radial distribution of cold plasma and monoenergetic beam, and the restriction of the analysis to the axialsymmetric TM modes.

In this framework, we have studied the exact electromagnetic structure linked to the presence of a plasma or a beam inside a perfect metallic waveguide and developed a model to investigate the possible couplings. We have shown that due to the finite thickness and non-negligible current density of the relativistic electron beam, the first slow modes can be distinguished. Because of this, coupling among several of them can appear with the first plasma mode. This analysis

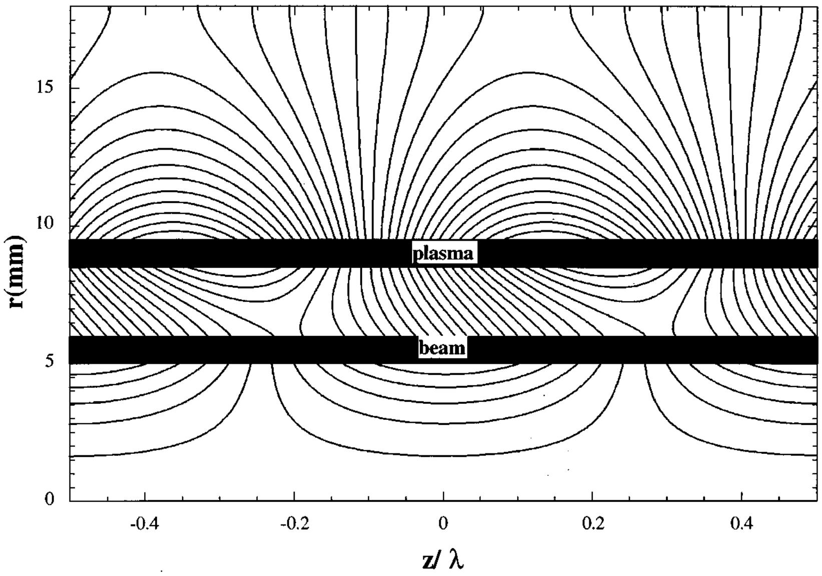

FIG. 19. Electric-field lines of the amplified wave on the scale of a wavelength corresponding to a frequency of 16.3 GHz. Other calculational parameters are the same as those of Fig. 9.

gives the opportunity to understand the dependence of the spatial growth rate versus frequency and plasma density, especially the sharp cutoff of the low-frequency spectrum, which takes place at a certain value of plasma density. Furthermore, this raises the possibility for the maser to work on several frequencies and, if so, may explain the experimental spectrum observed in other experiments. Finally, this opens the door to choose experimental parameters for a given regime of the maser in the framework of the assumptions described above. Also, the structure of the field has been investigated. A map of the field in the interaction region has been plotted. This document is of interest to foresee the behavior of the wave at the exit of the interaction region.

ACKNOWLEDGMENTS

The author would like to thank Jean-Max Buzzi, Yannick Caillez, and Oleg Loza for useful discussions. This work was in part supported by DGA-DRET Contract No. 40-95-007-00.

[1] M. Danos, S. Geschwind, H. Lashinsky, and A. Van Trier, Phys. Rev. **92**, 828 (1953).
[2] D. Bohm and E. Gross, Phys. Rev. **75**, 1851 (1949).
[3] A. I. Akhiezer and Ia. B. Fainberg, Dokl. Akad. Nauk SSSR **65**, 555 (1949).
[4] A. B. Kitsenko and K. N. Stepanov, Zh. Éksp. Teor. Fiz. **31**, 642 (1956) [Sov. Phys. JETP **4**, 512 (1957)].
[5] K. N. Stepanov and A. B. Kitsenko, Zh. Tekh. Fiz. **31**, 167 (1961) [Sov. Phys. Tech. Phys. **6**, 120 (1961)].
[6] M. V. Kuzelev and A. A. Rukhadze, *Basics of Plasma Free Electron Lasers* (Editions Frontières, Gif-sur-Yvette, 1995).
[7] M. V. Kuzelev, F. H. Muhametzianov, M. S. Rabinovitch, A. A. Rukhadze, P. S. Strelkov, and A. G. Shkvarunets, Zh. Éksp. Teor. Fiz. **83**, 1358 (1982) [Sov. Phys. JETP **56**, 780 (1982)].
[8] J. S. De Groot, R. A. Stone, and J. H. Rogers, Proc. SPIE **873**, 37 (1988).
[9] M. Birau, Thèse de doctorat, Université Paris VI, 1995 (unpublished).
[10] A. F. Alexandrov, M. V. Kuzelev, and A. N. Khalikov, Fiz. Plazmy **14**, 455 (1988) [Sov. J. Plasma Phys. **14**, 267 (1988)].
[11] T. D. Pointon and J. S. De Groot, Phys. Fluids **31**, 908 (1988).
[12] A. F. Alexandrov, L. S. Bogdankevich, and A. A. Rukhadze, in *Principles of Plasma Electrodynamics*, edited by G. Ecker, Springer Series in Electrophysics Vol. 9 (Springer-Verlag, Berlin, 1984).
[13] M. V. Kuzelev, F. H. Muhametzianov, and A. G. Shkvarunets, Fiz. Plazmy **9**, 1137 (1983) [Sov. J. Plasma Phys. **9**, 780 (1983)].
[14] A. I. Akhiezer, I. A. Akhiezer, R. V. Polovin, A. G. Sitenko, and K. N. Stepanov, *Plasma Electrodynamics* (Pergamon, New York, 1975), Vol. 1.
[15] D. Quémada, *Ondes dans les Plasmas* (Hermann, Paris, 1968).
[16] W. D. Jones, H. J. Doucet, and J.-M. Buzzi, *An Introduction to the Linear Theories and Methods of Electrostatic Waves in Plasmas* (Plenum, New York, 1985), p. 287.
[17] *Handbook of Mathematical Functions*, 9th ed., edited by M. Abramowitz and I. A. Stegun (Dover, New York, 1972), p. 18.
[18] M. Masuzaki, C. Y. Lee, R. Yamashita, R. Ando, and K. Kamada, in *Proceedings of the Tenth International Conference on High-Power Particle Beams, 1994, San Diego*, edited by W. Rix and R. White (National Technical Information Service, Springfield, 1994), p. 949.
[19] I. N. Onishchenko, D. Yu. Sidorenko, and G. V. Sotnikov, in *Proceedings of the Tenth International Conference on High-Power Particle Beams, 1994, San Diego* (Ref. [18]), p. 941.
[20] M. V. Kuzelev, A. A. Rukhadze, P. S. Strelkov, and A. G. Shkvarunets, Fiz. Plazmy **13**, 1370 (1987) [Sov. J. Plasma Phys. **13**, 793 (1987)].
[21] A. G. Shkvarunets, A. A. Rukhadze, and P. S. Strelkov, Fiz. Plazmy **20**, 682 (1994) [Plasma Phys. Rep. **20**, 613 (1994)].